PAPER

The multi-scale fusion reconstruction algorithm of CT and CL

Physica Scripta

PAPER

The multi-scale fusion reconstruction algorithm of CT and CL

RECEIVED
6 June 2023

REVISED
30 August 2023

ACCEPTED FOR PUBLICATION
15 September 2023

PUBLISHED
28 September 2023

Tong Jia[1,2,3], **Cunfeng Wei**[1,2,3], **Min Zhu**[4], **Rongjian Shi**[1,3], **Zhe Wang**[1,3], **Xindong Cui**[4,5] and **Baodong Liu**[1,2,3,*]

[1] Beijing Engineering Research Center of Radiographic Techniques and Equipment, Institute of High Energy Physics, Chinese Academy of Sciences, Beijing 100049, People's Republic of China
[2] School of Nuclear Science and Technology, University of Chinese Academy of Sciences, Beijing 100049, People's Republic of China
[3] Jinan Laboratory of Applied Nuclear Science, Jinan 250131, People's Republic of China
[4] CAS Key Laboratory of Vertebrate Evolution and Human Origins, Institute of Vertebrate Paleontology and Paleoanthropology, Chinese Academy of Sciences, Beijing 100044, People's Republic of China
[5] University of Chinese Academy of Sciences, Beijing 100049, People's Republic of China
[*] Authors to whom any correspondence should be addressed.

E-mail: liubd@ihep.ac.cn

Keywords: computed tomography, computed laminography, multi-scale fusion reconstruction algorithm, paleontological fossils, multilayer printed circuit boards

Abstract

Computed tomography (CT) is a widely used nondestructive testing (NDT) technique for material research, paleontology research and other fields. However, it is difficult for CT to reconstruct flat objects at high magnification ratios. Computed laminography (CL) enables high-resolution imaging for flat objects due to its unique scanning geometry. A challenging task for CL image reconstruction is to deal with the cross-section artifacts resulting from the incomplete projection data acquired from the CL scan. An effective multi-scale fusion reconstruction algorithm of CT and CL was proposed in this paper. The algorithm combining the advantages of the two scanning geometries, low-resolution CT data was used to compensate for the data missing in CL projection domain, and the cross-section artifacts were reduced. Experiments on paleontological fossils and multilayer printed circuit boards (PCB) were performed, where CT and CL data from different systems and scanning conditions. The results showed that the method can effectively suppress the cross-section artifacts of CL and obtain high-resolution reconstructed images.

1. Introduction

X-ray CT imaging is irreplaceable in medicine, industry, archaeological research and even security inspection. CT originated in the 1970s and was mainly used in biomedical fields at that time [1, 2]. Since the 1980s, CT has been popular in material analysis, structural analysis, defect detection [3, 4]. In the recent years, higher machining accuracy and defect detection of plate devices (such as PCB) are required in the development of aerospace, microelectronics and other industries. With the continuous development of archaeology, higher precision nondestructive testing instruments have gradually become an urgent need. Therefore, higher precision imaging is one of the main development directions in the field of NDT.

When CT scans a large flat object such as PCB and paleontological fossils, in order to avoid collision, the X-ray tube cannot get too close to the object. Furthermore, the X-ray energy must be high enough to penetrate the thickest direction of the object [5]. So, CT usually only can get a relatively low-resolution image of the object [6]. In a CL scanning, the X-ray source can always close to the flat object and the X-ray energy of CL does not need to be too high, so it can get reconstructed images with high spatial and contrast resolution. CL has been widely used in high resolution reconstruction of flat objects. The CL scanning setup adopted in our experiments is illustrated in figure 1 [7].

CL is a kind of CT with special architecture [8]. Due to the limited scanning angle, CL cannot obtain complete projection data, which results in serious cross-section artifacts in the reconstructed images.

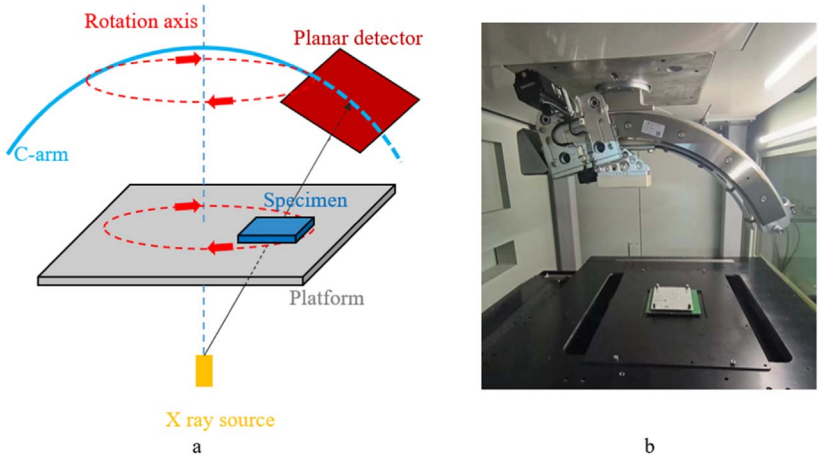

Figure 1. CL geometry. (a) The architecture of the CL system; (b) The CL equipment.

There are many researches on limited-angle problem, but many of them are filters and regularization algorithms designed based on the prior information of the scanned object itself [9, 10], including objects with the uniformity of material or regular internal shapes like circuit boards, etc But in many cases, the material distribution of objects is not uniform and the shape is irregular (such as fossils), so it is difficult for the algorithm relying on prior information to play a satisfactory effect.

Theoretically, low-resolution CT projection data with complete data can be used to compensate for the missing information in CL projection domain. In this paper, the idea of fusing CT and CL projection data is proposed to obtain high resolution reconstructed images with less artifacts. Different from algorithms that rely on prior information, fusion reconstruction does not need to use any prior information, so it can have better practicability.

In this work, we proposed a multi-scale fusion reconstruction algorithm based on ordered subset simultaneous algebraic reconstruction technique (OS-SART) [11]. The algorithm can not only unify the reconstruction resolution, but also greatly reduce the huge amount of computation caused by super-resolution reconstruction. At the same time, point cloud registration and energy calibration algorithms are introduced to solve the problem of projection data mismatch caused by different systems, which greatly improves the universality of the method. Fusion reconstruction can combine the advantages of CT and CL to make the reconstruction result better than either method. The experimental results showed that this method can significantly suppress the cross-section artifacts of CL, greatly improve the quality of reconstructed images, and has high application value.

This paper is organized as follows. In section 2, the whole flow of fusion reconstruction algorithm is given; the formula and algorithm details are introduced. The proposed method is validated by simulation as well as by application to actual datasets in section 3, respectively. Conclusions and discussion are given at the end of the paper.

2. Methodology

2.1. Multi-scale reconstruction algorithm

The consistency of CT and CL reconstruction image resolution is crucial for subsequent geometric registration, energy calibration and final fusion reconstruction. CL usually has a much higher resolution than CT. If the field of view (FOV) of a CT scan is reconstructed with the same voxel size as CL, the scale of the data and the computation cost are usually unacceptable. Fortunately, only the region of interest (ROI) which is much smaller than the FOV of the CT scan needs to be reconstructed with high resolution (called fine-grained reconstruction). In this work, a multi-scale reconstruction algorithm was developed. Fine-grained voxels were used in ROI and coarse-grained voxels were used in other regions. The example is shown in figure 2. The similar idea named mixed resolution reconstructions based on simultaneous iterative reconstruction technique (SIRT) [12] was used in ASTRA Toolbox [13].

The multi-scale reconstruction in this work was based on OS-SART algorithm. The realization method and formula of multi-scale reconstruction algorithm were shown below.

The coarse-grained global object is assumed to be f_G, and the ROI is marked with a mask f_{mask}, where f_{mask}=0 for voxels inside the ROI, and f_{mask}=1 for voxels outside the ROI. Then create a fine-grained 3D voxel

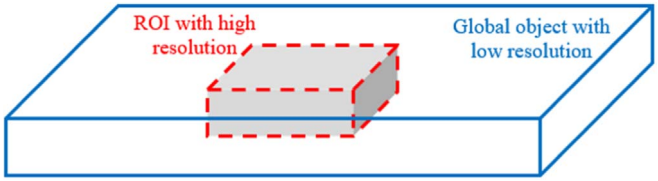

Figure 2. A multi-scale reconstruction algorithm example.

corresponding to the ROI and set it to f_H. The multi-scale OS-SART reconstruction formula is as follows:

$$f_{G_j}^{k+1/2} = f_{G_j}^{k} \times f_{mask_j}, \tag{1}$$

$$p_G^k = A_G f_G^{k+1/2}, \tag{2}$$

$$p_H^k = A_H f_H^k, \tag{3}$$

$$f_{G_j}^{k+1} = f_{G_j}^{k} - \lambda_G \frac{1}{a_{G_{+j}}} \sum_{i \in C_s} \frac{a_{G_{ij}}}{a_{G_{i+}}} (p_G^k + p_H^k - p), \tag{4}$$

$$f_{H_j}^{k+1} = f_{H_j}^{k} - \lambda_H \frac{1}{a_{H_{+j}}} \sum_{i \in C_s} \frac{a_{H_{ij}}}{a_{G_{i+}}} (p_G^k + p_H^k - p), \tag{5}$$

where $f_{G_j}^k$ is the value of j th voxel in coarse-grained global object, $f_{H_j}^k$ is the value of j th voxel in fine-grained ROI, k is the number of iterations. A_G and A_H are the system matrices of coarse-grained voxel and fine-grained voxel, respectively. p_G^k and p_H^k are the line integral of the coarse-grained voxel values and the fine-grained voxel values in the k th iteration, respectively. λ_G and λ_H are the relaxing factor, C_s is the projection subset, a_{+j} is the weight accumulation of the j th voxel in a projection subset, a_{i+} is the weight accumulation of the i th ray in a projection subset.

During the programming implementation of reconstruction algorithm, a_{i+} is usually defined as the length of reconstruction space traversed by ray, which means that $a_{H_{i+}}$ and $a_{G_{i+}}$ calculated in reconstruction space with different resolutions are inconsistent, which is incorrect in multi-scale reconstruction. So, it should be noted that in the multi-scale reconstruction formula, the sum $a_{H_{i+}}$ of the weights of ray I in formula (5) in the projection subset needs to be replaced by $a_{G_{i+}}$ in Formula (4).

2.2. Geometrical registration

To make the reconstructed objects coincide, the geometric coordinates of the two systems must be adjusted in the fusion reconstruction of CT and CL. The variety of scanned items made it challenging to automatically extract 3D attributes with accuracy. Also, it was challenging to automatically recognize and locate the feature structure of the objects due to cross-section artifacts of CL.

Rough registration was the initial phase of this work. For two independent CT and CL scanners, due to the difference in scanning geometry, the object reconstructed by them may be mirrored in a certain dimension, which cannot be registered only by rotation and shift, so it is necessary to manually adjust the parameters of the CT reconstruction system. Sometimes, due to the different starting angles of CT scanning, the CT reconstructed object may be perpendicular to the CL reconstructed object. It is also possible to manually adjust the reconstructed starting Angle to roughly align the areas of interest of CT and CL reconstructed results. These are all tasks that need to be carried out in the rough registration stage. Rough registration can not only reduce the difficulty of subsequent fine registration, but also improve the accuracy of the registration algorithm. Then the feature (such as the copper column, hole and fossil cracks, etc) of every reconstructed slice is extracted by edge extraction algorithm. All the extracted slice features were merged into three-dimensional features and convert them into point cloud data, then the closest point iteration (ICP) algorithm [14] was used for registration, as shown in figure 3. For calculating the transformation matrix (including rotation matrix and translation matrix), the ICP algorithm employed an iterative technique and gradually got closer to the ideal registration result. When the point cloud noise is minimal, the ICP algorithm can produce good results, but it is sensitive to the initial position of the calibrated point cloud.

It should be noted that if two scans (CT and CL) can be completed on the same scanner, the coarse registration is not necessary. Additionally, if the geometric parameters are exact enough, the fine registration stage might not even be necessary.

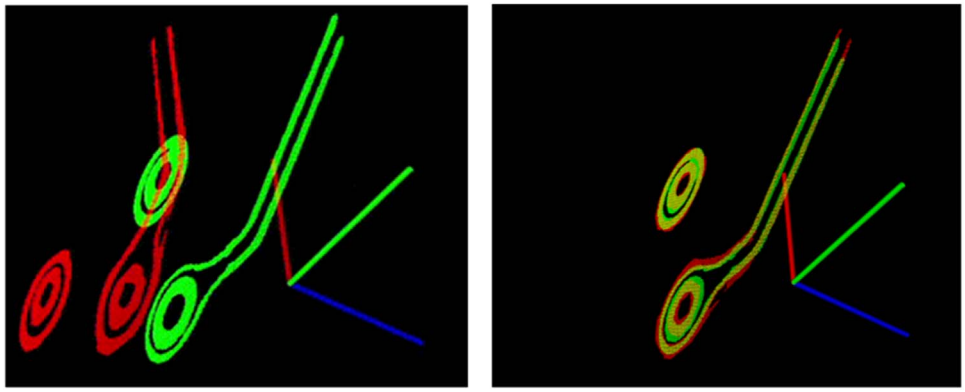

Figure 3. The left figure shows the two objects after rough registration and the right figure shows the result after fine registration with ICP algorithm.

2.3. Energy calibration

The linear attenuation coefficient of the reconstructed image is related to the X-ray energy, and the fusion reconstruction algorithm needs to ensure that the results reconstructed by CT and CL are consistent.

However, the projection data of CT and CL come from different scanning conditions, and the scanning trajectory and X-ray energy are greatly different. In addition, the X-ray usually has a wide energy spectrum and is easily affected by reconstruction artifacts (cross-section artifacts, scattering and beam hardening) [15], so it is difficult to accurately unify the results reconstructed by CT and CL.

After geometric calibration, objects were reconstructed respectively by CT and CL at the same resolution, and then the mean values of the same sub-regions were calculated respectively. Based on the average value of CT, a linear mapping relationship between CL line attenuation coefficient and projection data was established, thus completing energy calibration. Taking CT as an example, the calibration formula is as follows,

$$p'_{CL} = \frac{\overline{f'_{CT}}}{\overline{f'_{CL}}} \times p_{CL}, \tag{6}$$

where $\overline{f'_{CT}}$ represents the average value of the specified CT subregion, and $\overline{f'_{CL}}$ represents the average value of the specified CL subregion.

2.4. Multi-scale fusion reconstruction algorithm

After geometric registration and energy correction, the final multi-scale fusion reconstruction algorithm is the superposition of two multi-scale reconstruction algorithms that share the ROI.

In the multi-scale fusion reconstruction algorithm, the number of subsets divided by CT and CL is the same (the number of projection angles within subsets may be different, depending on the specific scanning strategy). CT and CL alternate forward and backward-projection, working together to update the fine-grained voxels in the ROI region. CT and CL renew the coarse-grained voxels in their own regions respectively.

The aforementioned procedure for multi-scale fusion reconstruction algorithm is summarized in Algorithm 1.

Algorithm 1 Multi-scale Fusion Reconstruction Algorithm

Input: Projection data p_{CT} and p_{CL}, the number of iterations N, the number of projection subsets S.
Output: Result of fusion reconstruction f_H.
1: Formula (1)-(5) was used to reconstruct CL and CT:
$[f_{G\_CL}, f_{H\_CL}] \leftarrow MultiScale\_SART(p_{CL}, N, S)$
$[f_{G\_CT}, f_{H\_CT}] \leftarrow MultiScale\_SART(p_{CT}, N, S)$.
2: ICP algorithm was used for registration and transformation matrix was obtained.
$matrix_{Trans} \leftarrow ICP(f_{H\_CT}, f_{H\_CL})$.
3: Geometrical registration
$[f'_{G\_CT}, f'_{H\_CT}] \leftarrow MultiScale\_SART(p_{CT}, matrix_{Trans}, N, S)$.
4: Energy calibration
$p'_{CL} \leftarrow \frac{subregion\_mean(f'_{H\_CT})}{subregion\_mean(f_{H\_CL})} \times p_{CL}$.
5: Fusion reconstruct:
for k in [0, N-1]
for s in [0, S-1]

(Continued.)

Algorithm 1 Multi-scale Fusion Reconstruction Algorithm

$[f_{G\_CL}, f_H^{k/2}] \leftarrow MultiScale\_SART\_oneSubset(p'_{CL}, s)$
$[f_{G\_CT}, f_H^{k}] \leftarrow MultiScale\_SART\_oneSubset(p_{CT}, matrix_{Trans}, s)$
end for
end for

Table 1. Simulation circuit board phantom scan parameters in CT and CL.

	Source to object distance	Source to detector distance	Detector unit size	Phantom size
CT	51 mm	710 mm	127 μm	1.1 μm
CL	7.89 mm	359.85 mm	49.5 μm	1.1 μm

Table 2. Reconstruction parameters of Simulation circuit board phantom.

	Number of reconstructed voxels	Number of projected pixels	Voxel size	Iterations
CT	1024 × 1024 × 190	512 × 512 × 360	1.1 μm	20
CL	1024 × 1024 × 190	1024 × 1024 × 360	1.1 μm	20
Fusion	1024 × 1024 × 190	512 × 512 × 360 1024 × 1024 × 360	1.1 μm	20

3. Results and discussion

This section first used a simulated circuit board phantom to demonstrate the cross-section artifact of CL and analyze the result of fusion reconstruction. The simulated PCB-phantom is made up of ten layers of various circuits spaced apart by air. Following that, multilayer printed circuit boards and ancient fish scales were used in tests using actual data.

3.1. Simulated circuit board phantom

Each circuit layer and air layer of the simulation circuit board phantom were 10 layers, the size of the phantom was 1024 × 1024 × 190 and the voxel size was 1.1 × 1.1 × 1.1 μm^3.

The scan and reconstruction parameters are shown in tables 1 and 2.

According to the calculation of amplification ratio, the minimum voxel that CT can actually reconstruct was 9.12 μm and CL can actually reconstruct was 1.08 μm. To facilitate comparison, the reconstructed voxel size was unified as 1.1 μm. Because the amount of data in the simulation experiment was small, the multi-scale algorithm was not used here.

Figure 4 displays the findings of the reconstruction. By contrasting figures 4(a)–(c), it is clear that CT reconstruction results are clearly blurred due to its inadequate amplification ratio and CL reconstruction results have significant cross-section artifacts, whereas fusion reconstruction significantly improves the quality of reconstructed images while preserving the longitudinal structure of objects.

In order to evaluate the performance of the proposed method, 1D profiles of the images reconstructed by different methods are shown in figure 5. We can see that the reconstructed gray values of the proposed method are more accurate.

As shown in the figure 6, the peak signal-to-noise ratio (PSNR) [16] and the structural similarity (SSIM) [17] were used to analyze the quality of CT, CL and fusion reconstruction.

Both SSIM and PSNR results of fusion reconstruction were significantly higher than those of CT and CL in figure 6. This shows that the fusion of the projection data of the two systems can make up for the defects of CT and CL respectively, so as to reconstruct results superior to those of either system.

3.2. Fish fossil

Fossils are the remains and moving remains of ancient animals and plants that have been compressed and deposited over a long period of time. They are usually encased in rocks, so the paleontological information preserved by fossils is mainly hidden inside them. In the earliest days of fossil research, researchers used grinding method [18] to analyze the internal structure of fossils. The grinding method involves cutting and grinding the

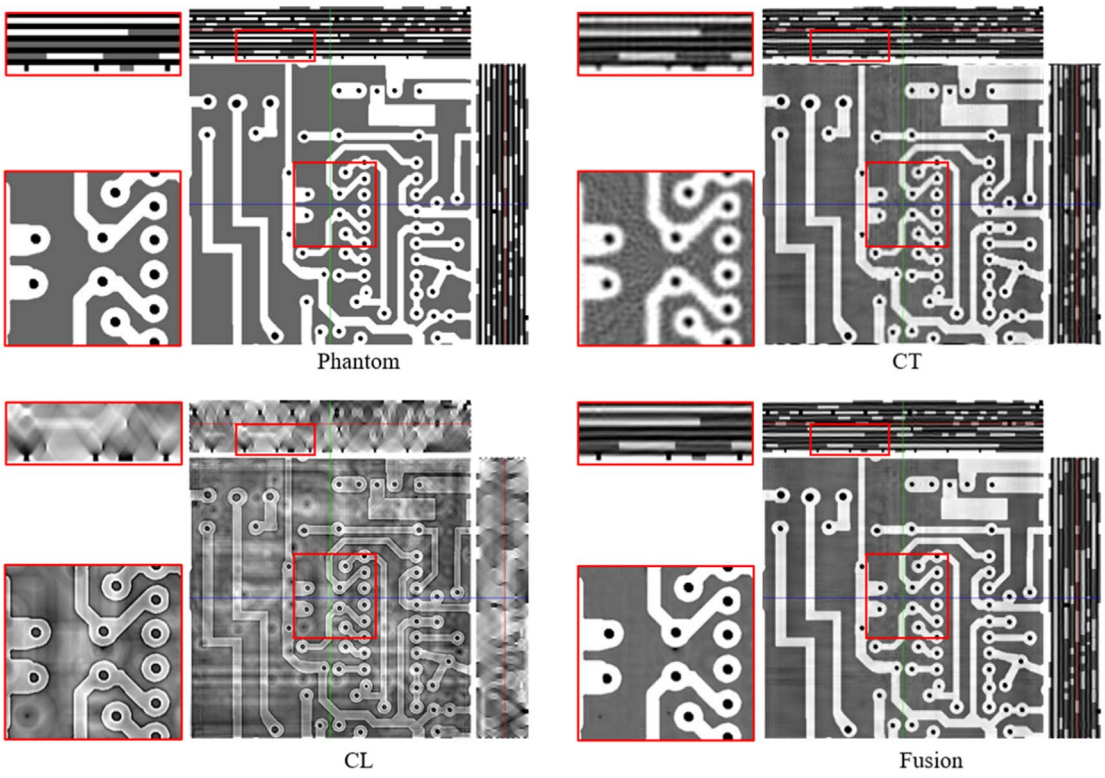

Figure 4. Simulated circuit board and the reconstruction results. The Phantom, CT and Fusion show the display windows [0, 1], and the CL show the display windows [0, 0.6].

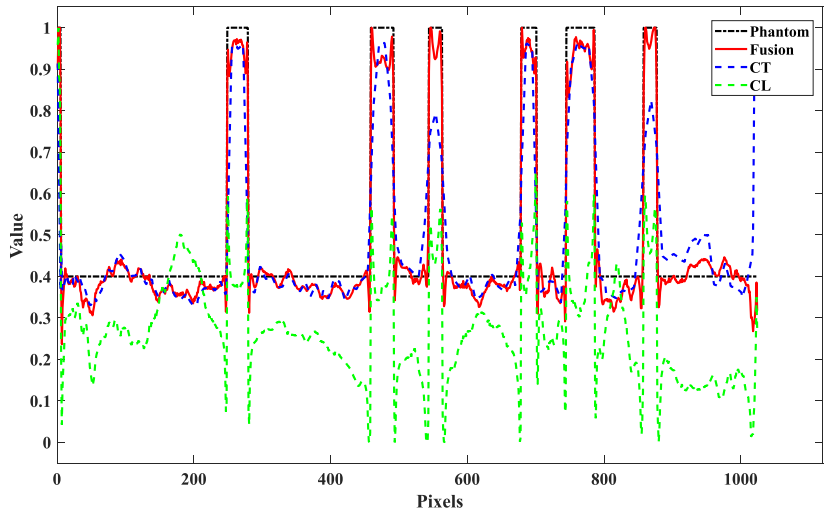

Figure 5. The reconstruction results were compared in line 450 of the 105th slice.

fossil layer by layer to observe and map the structure of the fossil site, and finally combining each layer to obtain 3D information about the fossil's interior. This method consumes a lot of manpower and requires a high technical level for operators. Meanwhile, the accuracy of the 3D structure of the fossil based on this method is also limited. Most importantly, this method destroys fossils, which has led to the popularity of nondestructive testing based on X-rays as an important tool in paleontological research.

Modern fish can use several behaviors to produce a large number of different activity traces, but such traces caused by fish cannot be fossilized for various reasons, and even if they are fossilized, they may be misinterpreted as activity traces of other organisms [19]. A better understanding of fish fossils is needed to better understand the marine and continental fossil records. Through the study of fish fossils, we can reconstruct the ancient fishes and

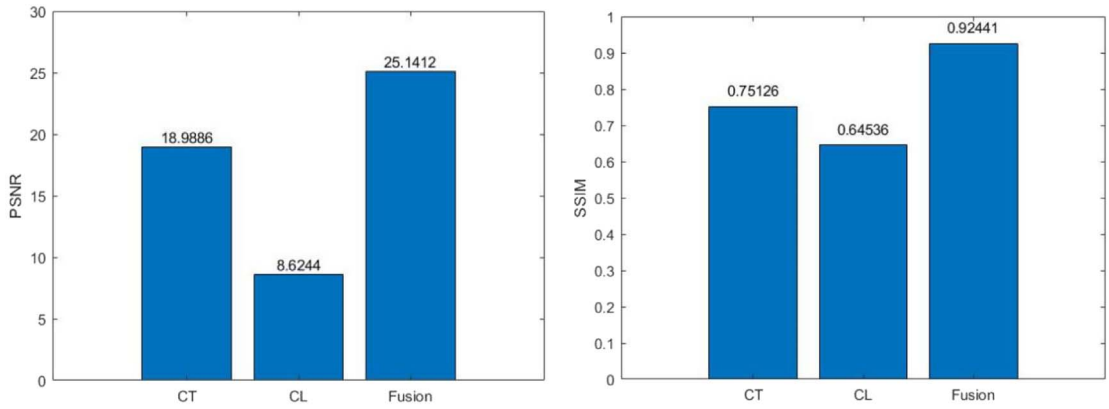

Figure 6. PSNR and SSIM of CT, CL and Fusion reconstruction results at the 104th layer.

Figure 7. Fossil of fish.

Table 3. Scanning parameters of fish scale fossils in CT and CL.

	Tube voltage	Tube current	Detector unit size	Detector cells	Exposure time	Number of views	Amplification ratio
CT	150 kV	120 μA	200 μm	2000 × 2000	1 s	1800	2.78
CL	90 kV	50 μA	127 μm	1920 × 1536	1 s	720	14.11

their related paleoenvironments, and infer the composition and origin of fishes in a specific period, which is of great significance to the study of marine fish paleobiogeography and reveal the evolution process of fishes [20].

As shown in figure 7, the projection data used here were CT and microscopic CL scans of a fish fossil with numerous scales. In this experiment, CT scanner is produced by GE (General Electric Company), CL scanner from the Institute of High Energy Physics of the Chinese Academy of Sciences.

As can be seen from table 3, X-ray penetration requires more energy because of the higher density of fossils. So, the X-ray tube power of CT is 4 times that of CL. Due to the flat shape of the fossil, the magnification ratio of CT is only 2.78 times, while that of CL can reach 14 times.

Table 4 shows the reconstruction parameters of fish scale fossils. According to the calculation of the amplification ratio in the scanning parameters, the minimum voxel size that CT scan reconstruct is about 72 μm, and CL can reconstruct the minimum voxel size is about 9 μm. The size of the voxel in the ROI region is the same for all three reconstruction approaches (CT, CL, and fusion reconstruction), but the size of the coarse-grained voxel in the other regions is dependent on the quantity of data that was actually computed. This is accomplished using a multi-scale reconstruction algorithm. Because the projection and reconstruction data are too big in fusion reconstruction, the coarse-grained size is further expanded in this experiment.

Figure 8 compares the outcomes of reconstructing fish scale fossils. The gray window range of CL in figure 8 differs from that of CT. This is due to the lower ray energy used for CL scanning compared to CT, which

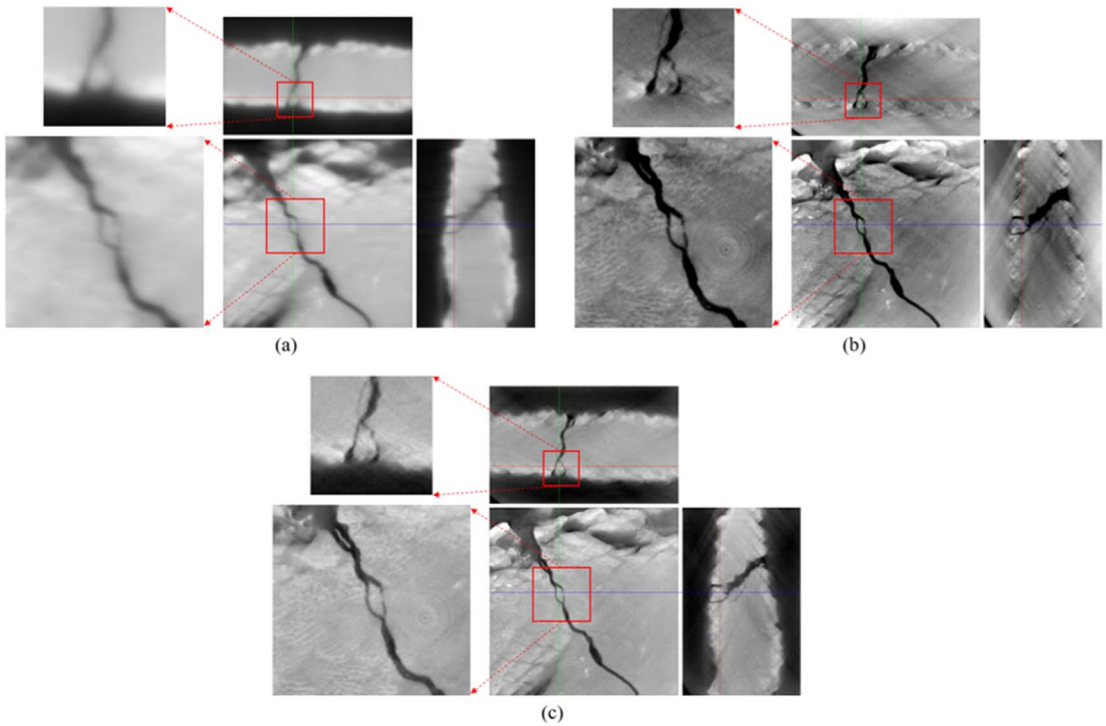

Figure 8. Comparison of fish scale fossil reconstruction results. (a) CT multi-scale reconstruction; (b) CL multi-scale reconstruction; (c) Multi-scale fusion reconstruction. The (a), (b) and (c) show the display windows [0, 0.11], [0, 0.16], and [0, 0.11], respectively.

Table 4. Reconstruction parameters of fish scale fossils.

	Coarse-grained voxels	Fine-grained voxels	Iterations
CT	2000 × 2000 × 1000 / 72 μm	1277 × 1277 × 800 / 9 μm	20
CL	800 × 800 × 656 / 36 μm	1277 × 1277 × 800 / 9 μm	20
Fusion	1000 × 1000 × 500 / 144 μm (CT) 550 × 550 × 200 / 72 μm (CL)	1277 × 1277 × 800 / 9 μm	20

produces results with a higher gray scale and a wider gray window range. The gray level of the fusion reconstruction findings was consistent with those of CT reconstruction since energy calibration on CL projection data was done before fusion reconstruction.

It can be seen from the overall three views figures 8(a)–(c) that the fusion reconstruction perfectly maintains the overall structure of CT and greatly reduces the cross-section artifacts of CL. By comparing the detail, it can be seen that the CT with the original resolution of 72 μm still could not reconstruct the fine cracks of the fossil after the super-resolution reconstruction of 9 μm. CL can show the cracks clearly. The results of fusion reconstruction retain the advantage of high resolution of CL, and the crack area is still very clear. For the fossil fish scale, the outer scale structure is one of the important parts to be studied. The cross-section artifacts of CL make it difficult to distinguish the scale structure from the external air. Meanwhile, the scale structure reconstructed by CT will miss a lot of details. By comparing the detail images figure 8 on the side, the results of fusion reconstruction are richer than those of CT reconstruction while retaining clear edge structures.

It can be seen that the effect of fusion reconstruction is better than either of CT and CL reconstruction. In the field of nondestructive testing of fossils, one of the main needs is to be able to segment the whole fossil and each part of the fossil at a high resolution. However, CT cannot meet the needs of detailed fossil segmentation, and CL cannot meet the needs of overall fossil segmentation. Fusion reconstruction is a viable option for dealing with this issue.

Due to the high density of the fossil itself, CT requires high-energy rays in order to penetrate the thickest part of the fossil, which will lead to poor density resolution of reconstructed images. CL can use low energy rays, so it has good density resolution. From the comparison of (a) and (b) in figure 9, it can be seen that the fossil

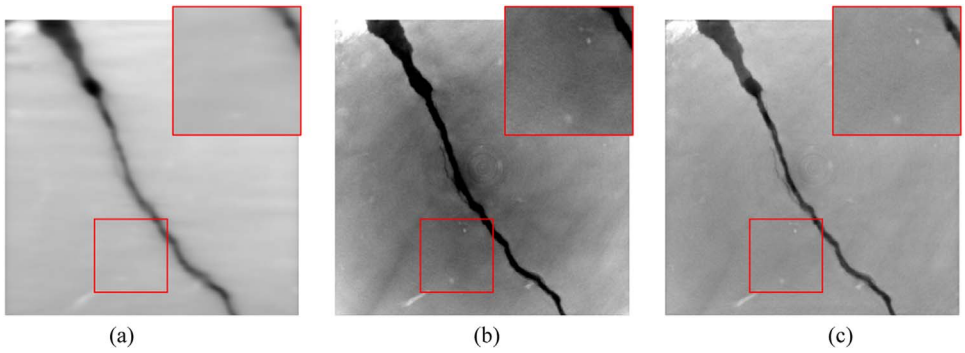

Figure 9. Contrast of white high-density dots. (a) CT multi-scale reconstruction; (b) CL multi-scale reconstruction; (c) Multi-scale fusion reconstruction. The (a), (b) and (c) show the display windows [0, 0.11], [0, 0.16], and [0, 0.11], respectively.

Figure 10. Photograph of the PCB and its internal structure.

Table 5. Multilayer PCB scan parameters in CT and CL.

	Tube voltage	Tube current	Detector unit size	Detector cells	Exposure time	Number of views	Amplification ratio
CT	90 kV	85 μA	127 μm	1024 × 1024	1 s	360	14.43
CL	110 kV	36 μA	49.5 μm	2940 × 2304	1 s	360	45

Table 6. Reconstruction parameters of multilayer PCB.

	Coarse-grained voxels	Fine-grained voxels	Iterations
CT	1240 × 1240 × 1240 / 8.8 μm	1727 × 1727 × 2000 / 1.1 μm	20
CL	1000 × 1000 × 500 / 4.4 μm	1727 × 1727 × 2000 / 1.1 μm	20
Fusion	1240 × 1240 × 1240 / 8.8 μm (CT) 1000 × 1000 × 500 / 4.4 μm (CL)	1727 × 1727 × 2000 / 1.1 μm	20

reconstructed by CL has a higher density of white dots. In figure 9(c), the results of fusion reconstruction also maintain the density resolution advantage of CL.

3.3. Multilayer printed circuit board

Miniaturization and integration have dominated the design of many electronic gadgets as a result of the industry's explosive growth in mobile internet use. The number of layers of PCB started to stack as well as the precision and complexity of the PCB manufacturing process rose year after year in order to boost the effectiveness of space utilization. In order to assess the correctness of circuit board fabrication, NDT is becoming more and more crucial [21]. The PCB wiring, drilling, and other machining accuracy information may be accurately and effectively obtained from a high-precision reconstructed image, which is of considerable relevance for the advancement and iteration of its machining technology. The experiment of multiscale fusion

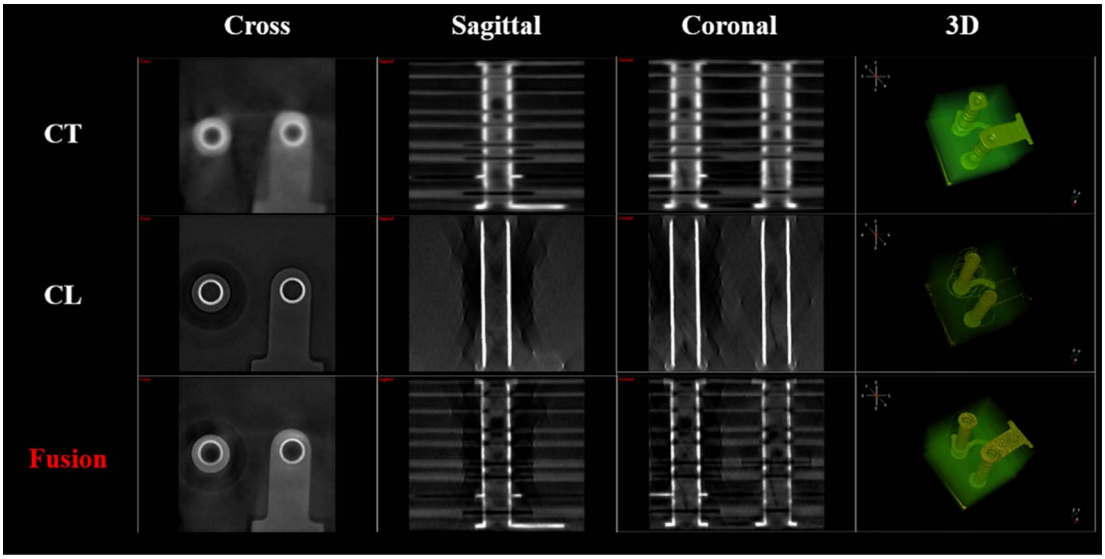

Figure 11. Comparison of multilayer PCB reconstruction results. The display windows are [0, 1.15].

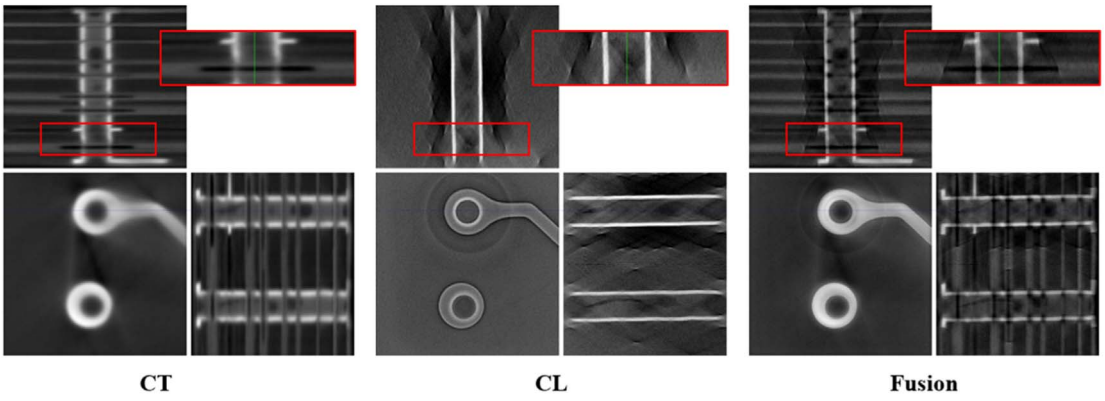

Figure 12. Comparison of multilayer PCB reconstruction results. The display windows are [0, 1.5].

reconstruction for multilayer PCB was carried out in this work. In this experiment, both CT and CL scanner are from the Institute of High Energy Physics of the Chinese Academy of Sciences.The PCB used in the experiment and its internal structure are shown in figure 10.

As can be seen from table 5, because PCB is simpler to penetrate than fossils, and the circuit boards used in the experiment are smaller in size, CT and CL reconstruction accuracy is quite high, among which the size of CL per voxel is only 1.1 μm.

Table 6 is the reconstruction parameters of multi-layer PCB, and the meanings of each parameter are the same as table 4. The fine-grained voxel size of ROI was 1.1 μm. OS-SART algorithm was used for 20 iterations of the reconstruction results, and the reconstruction results of the fine-grained ROI in the three reconstruction methods were compared at last. The following images compares the ultimate outcomes.

The comparison of reconstruction results of multi-layer circuit board is shown in figure 11. It can be seen from the three views of the PCB that the cross-section artifacts of CL make it impossible to see the interlayer structure of the PCB, and only two through-holes can be seen. However, the copper wire reconstructed by CL is clearer than CT. While fusion reconstruction keeps the reconstructed object clear, it greatly reduces the cross-section artifacts, and completely reconstructs the interlayer structure of PCB. Especially for the copper structure found inside the circuit board, fusion reconstruction offers greater accuracy and clarity.

As shown in figure 12, the area circled in red is the part of circuit board through hole disconnection. CL cannot reconstruct the information of longitudinal copper column disconnection, but fusion reconstruction restores this structural feature with the projection data of CT.

4. Conclusion

In this study, a multi-scale fusion reconstruction technique of CT and CL was developed. This algorithm effectively suppressed the interlayer structure missing and cross-section artifacts brought on by insufficient data in CL reconstruction. Through the actual data experiment of fish scale fossil and multi-layer PCB, it could be seen that the result of fusion reconstruction was superior to either of CT and CL in structure or in detail, which fully proves the effectiveness of fusion reconstruction. In addition, the CT and CL projection data used in this paper come from two different scanner, which also verifies the universality and practical value of the algorithm.

The fusion algorithm put forward in this research can be used to more diverse fields, such as the fusion reconstruction of CT data with two distinct resolutions, which can be utilized to lessen reconstruction truncation artifacts. The benefits of the reconstruction outcomes under various scanning trajectories can also be combined through the fusion reconstruction of CT data from various robotic arms.

The iterative reconstruction algorithm requires more computation, while the computation of fusion reconstruction was about 3 times that of ordinary iterative reconstruction under the condition of the same amount of data. Consequently, the primary issue that should be considered in this approach is the reconstruction time cost. This technique has many potentials uses in disciplines like paleontology and the detection of critical component defects that are not time-sensitive.

Acknowledgments

We thank Pengfei Yin and Yemao Hou for help with the CL and CT scan of the fish fossil (IVPP).

This work was supported in part by the National Key Research and Development Program of China under Grant 2017YFF0107201, in part by the CAS Interdisciplinary Innovation Team under Grant JCTD-2019-02, in part by the Strategic Priority Research Program of Chinese Academy of Sciences (XDA19050102 and XDB26000000) and in part by the National Natural Science Foundation of China (42130209).

Data availability statement

The data cannot be made publicly available upon publication because no suitable repository exists for hosting data in this field of study. The data that support the findings of this study are available upon reasonable request from the authors.

ORCID iDs

Tong Jia https://orcid.org/0000-0002-1873-7356

References

[1] La Rivière P J and Crawford. C R 2021 From EMI to AI: a brief history of commercial CT reconstruction algorithms *Med. Imag.* **8** 052111
[2] Fang Z, Hu W, Wang R and Chen S 2019 Application of hyperspectral CT technology combined with machine learning in recognition of plastic componentss *NDT and E Int.* **102** 287–94
[3] Zuber M *et al* 2017 Augmented laminography, a correlative 3D imaging method for revealing the inner structure of compressed fossils *Sci. Rep.* **7** R29–28
[4] Chiffre L D, Carmignato S, Kruth J P, Schmitt R and Weckenmann A 2014 Industrial applications of computed tomography *CIRP Ann - Manuf Technol* **63** 655–77
[5] Yunsong Z *et al* 2018 Edge information diffusion based reconstruction (EIDR) for cone beam computed laminography *IEEE Trans. Image Process.* **27** 4663 –75
[6] Wei Zenghui *et al* 2017 A micro-CL system and its applications *The Review of scientific instruments* **88** 115107
[7] Liu B *et al* 2015 An industrial computed laminography imaging System[C]*// Digital Industrial Radiology and Computed Tomography (DIR)* **20** 22–5
[8] Fisher S L, Holmes D J, Jørgensen J S, Gajjar P, Behnsen J, Lionheart W R B and Withers P J 2019 Laminography in the lab: imaging planar objects using a conventional X-ray CT scanner *Measurement Science and Technology* **30** 12
[9] Yu L *et al* 2014 Exploring the limits of limited-angle computed tomography complemented with surface data *European Conference on Non-Destructive Testing* **36** 8
[10] Wei Z *et al* 2018 A joint reconstruction and segmentation method for limited-angle X-ray tomography *IEEE Access* **6** 7780 –91
[11] Wang G and Jiang M 2004 Ordered-subset simultaneous algebraic reconstruction techniques (OS-SART) *J. X-Ray Sci. Technol.* **12** 169–77
[12] Gregor J and Benson T 2008 Computational Analysis and Improvement of SIRT *IEEE Transactions on Medical Imaging* **27** 918 –24
[13] van Aarle W *et al* 2015 The ASTRA toolbox: a platform for advanced algorithm development in electron tomography *Ultramicroscopy* **157** 35–47

[14] Besl Paul J and McKay Neil D 1992 A method for registration of 3-D shapes *IEEE Transactions on Pattern Analysis and Machine Intelligence* **14** 239–56
[15] Midgley S 2006 Energy resolution for accurate measurements of the X-ray linear attenuation coefficient *Radiat. Phys. Chem.* **75** 936–44
[16] Sidky E Y, Kao C-M and Pan X 2006 Accurate image reconstruction from few-views and limited-angledata in divergent-beam CT *J. X-Ray Sci. Technol.* **14** 119–39
[17] Wang Zhou *et al* 2004 Image quality assessment: from error visibility to structural similarity *IEEE transactions on image processing: a publication of the IEEE Signal Processing Society* **13** 600–12
[18] Joy K W, Willis A J and Lacey W S 1956 A rapid cellulose peel technique in palaeobotany *Annals of Botany* **20** 635–7
[19] Carcamo Carolina *et al* 2015 Cruziana- and rusophycus-like traces of recent sparidae fish in the estuary of the piedras river (Lepe, Huelva, SW Spain) *Palaeogeography, Palaeoclimatology, Palaeoecology: An International Journal for the Geo-Sciences.* **439** 176–83
[20] Mitsui S *et al* 2021 Fossil fish otoliths from the chibanian miyata Formation, kanagawa prefecture, Japan, with comments on the paleoenvironment *Geobios* **64** 47–63
[21] Tao W *et al* 2020 Machining accuracy detection of PCB hole by X-ray micro-CT *Micron* **131** 102826